TOWARD SMART AIR MOBILITY: CONTROL SYSTEM DESIGN AND EXPERIMENTAL VALIDATION FOR AN UNMANNED LIGHT HELICOPTER

Emanuele L. de Angelis[*,a,1], Fabrizio Giulietti[a,2], Gianluca Rossetti[b,3], Matteo Turci[b,4], Chiara Albertazzi[c,5]

[a] *University of Bologna, Department of Industrial Engineering (DIN), CIRI Aerospace, Forlí, Italy 47121*
[b] *Zephyr S.r.l., Forlí, Italy 47121*
[c] *Curti Costruzioni Meccaniche S.p.A., Castel Bolognese, Italy 48014*

Abstract

Light helicopters are used for a variety of applications, attracting users from the private and public market segments because of their agility and convenient storage capabilities. However, most light helicopters on the market today are designed and manufactured with technologies dating back to the 1980s, with safety issues to be addressed by advanced design methods, more powerful engines, and innovative solutions. In this regard, the DISRUPT (Development of an innovative and safe ultralight, two–seater turbine helicopter) project, lead by Curti Aerospace Division (Italy) and co–funded by EU H2020 program, represents a state–of–the–art concept for a novel ultralight helicopter, equipped with a ballistic parachute.

In order to validate the first parachute ejection in a safe scenario, a dronization process was selected as a viable solution to be performed in collaboration with the University of Bologna. In the present paper, the steps followed to transform the helicopter into an unmanned vehicle are detailed according to the Model–Based Design approach, with particular attention to the mathematical modeling, the control system design, and the experimental validation. Obtained results also demonstrate the feasibility of using a civil helicopter first as a remotely–piloted system and then as an highly–automated personal transportation system, in the direction of smart and sustainable air mobility.

1. INTRODUCTION

In the past decade technologies allowing for safe and efficient operations in urban areas for manned and unmanned aircraft systems earned a great interest in the scientific community. Two early attempts that investigated concepts of operation and technologies for a new personal transportation system based on both an aerial platform and a ground infrastructure were PPlane (2009–2013) and myCopter (2011–2014), projects funded by the European Commission under the 7th Framework Program (FP7).[1],[2]

The interest in the Urban Air Mobility (UAM) had a step increase over the last few years.[3] On the one hand the slow growth rate of ground infrastructures led to a critical traffic congestion in urban areas. On the other hand the increasing demand for moving people and payloads further and faster drove the attention of research community and stakeholders toward the exploitation of the vertical dimension.[4] In this respect, Amazon and Google pioneered the testing of urban parcel delivery by means of multirotor aircraft.[5],[6] In such a way, they paved the way for a wide range of studies on highly–automated low–altitude vehicles as an alternative means for transportation, where “the regular Joe” is capable to perform a mission without having the skills of a licensed pilot.[7],[8],[9]

In the same context, taking advantage of the consolidated state of the art of conventional aviation, the high reliability of onboard systems and avionics, and the fast increasing of electrical propulsion systems performance, main aircraft manufacturers and transport stakeholders (such as Airbus, Volocopter, and Uber) investigated concepts of personal air transportation systems. With the aim to play a lead role in this new raising market, electrical air platforms with Vertical Take–Off and Landing (VTOL) capabilities are being considered as the key elements for the next generation of controlled airspace.[10],[11]

Among all the above–mentioned projects and applications, it is acknowledged that a cost–effective solution to sustainable Urban Air Mobility and Delivery (UAMD)

---

[*] Corresponding author
[1] Assistant Professor, emanuele.deangelis4@unibo.it
[2] Associate Professor, fabrizio.giulietti@unibo.it
[3] Senior Research Engineer, gianluca.rossetti@zephyraerospace.com
[4] Senior Research Engineer, matteo.turci@zephyraerospace.com
[5] Helicopter Project Manager, c.albertazzi@curti.com

is represented by the use of small/light aircraft where onboard flight control systems, supported by Air Traffic Management (ATM) technology, will provide safe navigation in dynamic operational scenarios and weather conditions in the presence of other sky users.[12] In this respect, transforming an existing light conventional aircraft (both fixed and rotary–wing) into a Remotely–Piloted Aerial System (RPAS) may represent a successful strategy. First of all, available light/ultralight conventional aircraft already passed through several design, test, and certification steps, with the aim of fulfilling reliability, performance, and flying quality requirements.[13] Moreover, reversible conventional control chains can be easily replaced by Electro–Mechanical Actuators (EMA), controlled by dedicate onboard avionics. Starting from this design bias, researchers can thus focus more on the design and experimental validation of all the other technologies allowing for UAMD, including GNC, telemetry, communication, and ATM devices, in addition to ground handling facilities. In this regard, thanks to the compact size and the peculiar VTOL configuration, civil ultralight helicopters represent suitable test–beds for performing the transition toward a highly–automated personal transportation system.

By focusing on the very recent past, examples of transitions of conventional helicopters into RPASs can be dated back to 2004, when the Unmanned Little Bird demonstrator, which Boeing built from a civilian MD 530F, made its first autonomous flight (with safety pilot). In particular, a pre–programmed 20–minutes armed intelligence, surveillance, and reconnaissance mission was performed around the United States Army's Yuma Proving Ground facility.[14] In 2006 Northrop Grumman introduced the MQ–8 Fire Scout unmanned helicopter family, derived from Schweizer 333 and Bell 407, designed to provide reconnaissance, situational awareness, aerial fire and precision targeting support for ground, air, and sea forces.[15] In 2008 an unmanned highly–automated version of the Kaman K–MAX helicopter took its maiden flight, with the aim to operate in combat scenarios to deliver supplies to the battlefields, as well as in civilian situations involving chemical, biological, or radiological hazards.[16] Later on, Eurocopter launched a series of flights for a new rotary–wing solution designed to expand the mission capabilities of Eurocopter helicopters.[17] The Optionally Piloted Vehicle (OPV) program, based on EC145 helicopter platforms (now Airbus Helicopters H145), was revealed during a demonstration flight: after an automatic takeoff, an EC145 flew the circuit via multiple pre–programmed waypoints, during which the helicopter performed a mid–route hover to deploy a load from the external sling. The EC145 continued on a return route segment representing a typical observation mission, followed by an automatic landing. Finally, Sikorsky demonstrated its OPV Matrix Technology on a modified S–76B helicopter called Sikorsky Autonomy Research Aircraft (SARA). Since 2013 the program made progress with more than 300 hours of autonomous flight, with the aim to improve decision aiding for manned operations while enabling both unmanned and reduced crew operations.[18]

This paper presents the results of a research work performed within DISRUPT (2016–2018), a collaborative project co–funded by the EU within the H2020 program and led by Curti Aerospace Division. Specifically, DISRUPT proposed a new light helicopter configuration, the two–seater Curti Zefhir helicopter, that features a turbine engine and an emergency ballistic parachute to respectively enhance flight performance and increase passengers safety (see Figure 1). PBS Velká Bíteš manufactures the Zefhir's turboshaft, derated from 160 to 105 kW maximum continuous power. While ballistic parachutes have been certified on some fixed–wing aircraft, such as Cirrus light airplanes, installing them on helicopters is a trickier proposition due to the overhead presence of rotating blades. Contained in a non–rotating pod above the main rotor, the parachute solution proposed by Curti and Junkers ProFly thus becomes a backup for conditions where autorotation cannot be performed, such as a) flight control failure or loss of maneuverability, b) flying over an area where emergency landing cannot be safely performed, or c) flight conditions that prevent restoring rotor rotation speed.[19]

Figure 1: Zefhir helicopter (courtesy of Curti Aerospace Division).

Although the main objectives of DISRUPT were not strictly related to the main topics of UAM, the need for a remotely–piloted configuration arose immediately: since the experimental validation of the parachute system with the full scale helicopter was one of the main expected results, the transition toward an unmanned configuration became a mandatory activity to perform the ejection test without a human pilot on board. A crucial but challenging step toward such transition was the design of a stabilization system. Helicopters generally show a nonlinear complex dynamics that might manifest some unstable flight characteristics in limited zones of the flight envelope. In the particular case of a radio–controlled rotorcraft, without the direct perception of linear accelerations and attitude motion, the remote piloting of an helicopter is indeed an extremely hazardous task.[20],[21] Hence, an Automatic Flight Control System (AFCS) was designed, tested, and implemented, allowing the pilot to safely control the aircraft in terms of desired attitude.

The main goal of the paper is to present for the first time the detailed description of all the phases allowing the successful transition of a conventional light helicopter into a RPAS, stemming from the DISRUPT project. According to the Model–Based Design (MBD) philosophy, 1) mission requirements are defined and 2) hardware selection is performed. Then, 3) an accurate 6DOF nonlinear model is implemented in the Matlab/Simulink environment, which includes helicopter subsystems, environmental effects, and sensor and actuators behavior. 4) The mathematical model is then validated and refined by using flight data collected during an extensive experimental campaign. 5) After the analysis of open loop dynamic modes, 6) an attitude control system allowing the remote pilot to easily control the aircraft is designed, implemented, and validated by means of both 7) Hardware–In–the–Loop (HIL) techniques and 8) flight tests.

The paper is structured as follows. Section 2 addresses the definition of mission requirements and the selection of components. The entire simulation model, the trim and stability analysis, and the model validation procedure are presented in Sections 3 and 4, respectively. Control system design, implementation, and its HIL validation are described in Section 5. Experimental results validating the AFCS performance and reporting the parachute recovery mission are finally summarized in Section 6. A section of concluding remarks ends this paper.

The successful outcome of the ejection test and the interest arisen in several journals and broadcast media prove the relevance of the research activity presented in this paper.[22],[23] Zefhir is currently the only civil helicopter equipped with a ballistic parachute. Indeed, such a test has never been filmed or documented in the entire history of aerospace technology. However, due to the highly–classified nature of the data involved in an early stage of the aircraft development, a detailed description of helicopter features and of both numerical and experimental results is omitted in the present framework. The focus of the analysis is thus posed on the description of methodological aspects, with particular attention to both numerical and experimental validation, supported by results available in the literature. Also, the comparison between experimental data and the results of simulations is possibly characterized in terms of relative errors, while the description of technological setup is limited to functional aspects.

2. MISSION REQUIREMENTS AND COMPONENTS SELECTION

2.1. Mission requirements

Mission systems and subsystems are grouped into the ground segment and the flight segment:

- Ground segment or Ground Control Station (GCS): the complete set of ground–based hardware systems used to control and monitor the flight segment. The main components include the human–machine interface, computer, telemetry, and aerials for the control, video, and data link to/from the unmanned vehicle.
- Flight segment: the helicopter equipped with the necessary avionics to perform a remotely–piloted flight. The main components include sensors, actuators for rotors blade pitch angle control, onboard computer, and aerials for the control, video, and data link to/from the ground segment.

The final mission is defined by the following phases:

1. Pre–flight checks: the systems involved in the mission are prepared and visually–checked. The helicopter is placed on flat terrain at a safety distance from the GCS. The airfield is required to be clear of obstacles while the mission airspace is characterized by a radius of 5 km and height of 500 m with respect to the GCS.
2. Avionics power–on: both the ground and the flight segment subsystems are activated. Telemetry data are received by the GCS and software/hardware verification checks are performed. The pilot validates the correct actuation of control commands.
3. Engine start: the ignition procedure is remotely started by pilot's action and the turbine reaches the idle condition.
4. Take–off and climb: the helicopter takes–off and climbs out of ground effect at a controlled rate until reaching 300 m above the airfield.
5. Cruise: the helicopter is stabilized in steady level flight at about 30 kts.

6. Engine shutdown and parachute ejection: the pilot performs a termination procedure, which includes engine shutdown and parachute ejection.
7. Descent: the helicopter descends with a stabilized speed and lands within the prescribed area.

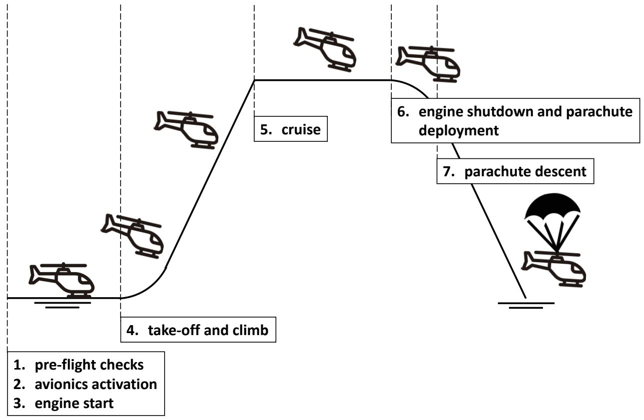

Figure 2: Mission phases definition.

The mission is performed in visual line of sight. However, telemetry information need to be available to both the GCS crew and the pilot. Given the intrinsic dynamic instability of the helicopter, fuselage attitude stabilization algorithms are required to assist the pilot throughout the mission profile. Conversely, no closed–loop control is applied to MR collective pitch. The use of an independent Flight Termination System (FTS) is mandatory to stop the engine in case of emergency.

2.2. Components selection

The selection of components for both the ground and the flight segments is performed according to the preliminary analysis of mission requirements. At the same time, the MBD approach is adopted to define systems and subsystems as the result of an iterative process, where the making of a simulation model represents the core of the control system development (see Sections 3 and 5). In what follows, the final selection list is presented while the unmanned system layout is sketched in Figure 3.

The GCS is made of:

- the control module, where a modified commercial–off–the–shelf Radio Controller (RC) is used as a human–machine interface. Commands by the pilot, represented by stick movements and switch activation inputs, are generated as Pulse–Width Modulated (PWM) signals and then collected according to Pulse–Position Modulation (PPM) protocol. The PPM signal is finally provided to an integrated microcontroller board and output to the communication module according to serial protocol;
- the monitoring module, represented by a rugged laptop, where a graphical user interface is designed to display telemetry data, plan the mission, and send high–level commands via ethernet TCP/IP connection to a Real–Time Computer (RTC1) for data acquisition and processing;
- the communication module, which provides RX/TX radio link to the flight segment. An ethernet switch is used to collect data from the monitoring module, while a ground–based radio modem is connected to a pair of 8 dBi 2.4 GHz directional patch antennas (respectively characterized by right–hand circular and vertical polarization).

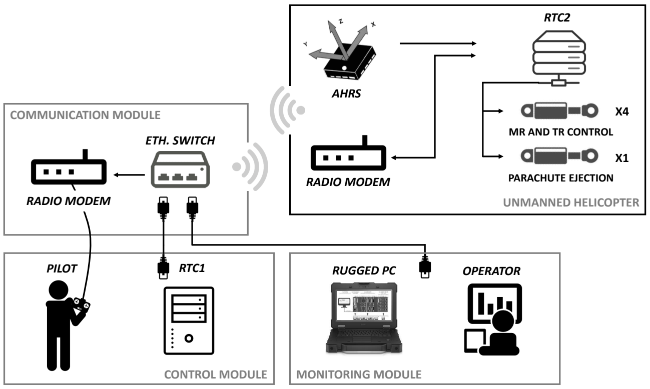

Figure 3: The unmanned system setup.

The helicopter is equipped with:

- a corresponding radio modem. Data are output via serial protocol and converted to a widespread standard industrial bus for communication with the Flight Management System (FMS);
- a high–performance Real–Time Computer (RTC2) integrating the FMS data acquisition and control tasks;
- a combined navigation and Attitude and Heading Reference System (AHRS) used to measure stabilized attitude information in a dynamic environment, along with position and velocity. Data are output via serial protocol and converted to a widespread standard industrial bus for communication with the FMS.
- a set of 4 EMAs control the collective, lateral, and longitudinal blade pitch of the MR and the collective pitch of the TR. Another EMA is used for parachute deployment actuation. An FTS, based on an independent 868 MHz radio system, allows

the Fuel Shut–Off Valve (FSOV) to close for an emergency engine shutdown. The EMA and FTS selected for the experiment are devices available in the civil market.

3. SYSTEM MODELING

Starting from the definition of reference frames, a 6 degrees–of–freedom model is adopted to represent the helicopter, with general expressions for the kinematics and dynamics of a rigid body with center of gravity CG.

3.1. Reference frames

Three right–handed orthogonal reference frames are introduced, according to the definitions in:[24]

1. an Earth-fixed North-East-Down frame, $\mathcal{F}_E = \{O_E; \boldsymbol{x}_E, \boldsymbol{y}_E, \boldsymbol{z}_E\}$: the origin, O_E, is arbitrarily fixed to a point on the Earth's surface, $\boldsymbol{x}_E$ aims in the direction of the geodetic North, $\boldsymbol{z}_E$ points downward along the Earth ellipsoid normal, and $\boldsymbol{y}_E$ completes a right-handed triad. This frame is assumed to be inertial under the assumption of flat and non–rotating Earth;

2. a Local Vertical Local Horizontal frame, $\mathcal{F}_H = \{CG; \boldsymbol{x}_H, \boldsymbol{y}_H, \boldsymbol{z}_H\}$: the origin is located at the vehicle center of gravity, CG. Under the hypothesis of flat Earth, $\mathcal{F}_H$ has axes parallel to $\mathcal{F}_E$;

3. a Body-fixed frame, $\mathcal{F}_B = \{CG; \boldsymbol{x}_B, \boldsymbol{y}_B, \boldsymbol{z}_B\}$: the $\boldsymbol{x}_B$–axis is positive out the nose of the rotorcraft in its plane of symmetry, $\boldsymbol{z}_B$ is perpendicular to $\boldsymbol{x}_B$ in the same plane of symmetry, pointing downwards, and $\boldsymbol{y}_B$ completes a right-handed triad;

4. an aircraft reference frame, $\mathcal{F}_A = \{O_A; \boldsymbol{x}_A, \boldsymbol{y}_A, \boldsymbol{z}_A\}$, used to locate CG and all helicopter components: the axes are parallel to the body–fixed frame axes, such that $\boldsymbol{x}_A = -\boldsymbol{x}_B$, $\boldsymbol{y}_A = \boldsymbol{y}_B$, and $\boldsymbol{z}_A = -\boldsymbol{z}_B$. The origin is located ahead and below the rotorcraft at some arbitrary point within the plane of symmetry. Stations (ST) are measured positive aft along the longitudinal axis. Buttlines (BL) are lateral distances, positive to the pilot's right, and waterlines (WL) are measured vertically, positive upward. A sketch of the rotorcraft including the selected $\mathcal{F}_A$ frame is reported in Figure 4. The positions of main components, expressed in $\mathcal{F}_A$, are listed in Appendix 1 together with relevant helicopter data.

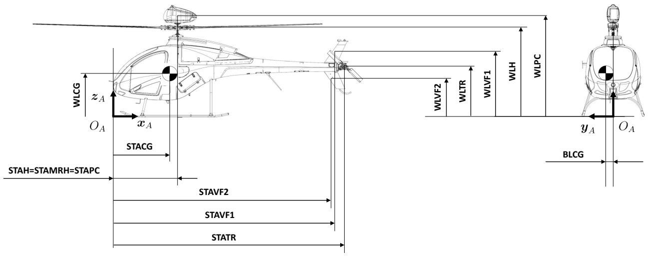

Figure 4: Sketch of the helicopter (courtesy of Curti Aerospace Division).

Let $s\left(\cdot\right) = \sin(\cdot)$, $c\left(\cdot\right) = \cos(\cdot)$. Vector transformation between $\mathcal{F}_H$ and $\mathcal{F}_B$ is provided by the rotation matrix[12]

$$(1) \qquad \boldsymbol{R}(\boldsymbol{\alpha}) = \begin{bmatrix} c\theta\, c\psi & c\theta\, s\psi & -s\theta \\ s\phi\, s\theta\, c\psi - c\phi\, s\psi & s\phi\, s\theta\, s\psi + c\phi\, c\psi & s\phi\, c\theta \\ c\phi\, s\theta\, c\psi + s\phi\, s\psi & c\phi\, s\theta\, s\psi - s\phi\, c\psi & c\phi\, c\theta \end{bmatrix}$$

obtained by a 3-2-1 rotation sequence where $\boldsymbol{\alpha} = [\phi,\, \theta,\, \psi]^T$ describes the attitude of the rotorcraft in terms of the classical 'roll', 'pitch', and 'yaw' angles, respectively. The following notation is adopted: if $\boldsymbol{w}$ is an arbitrary vector, its components are transformed from $\mathcal{F}_H$ to $\mathcal{F}_B$ through the relation $\boldsymbol{w}_B = \boldsymbol{R}\,\boldsymbol{w}_H$. In what follows, the subscript B will be dropped for simplicity.

3.2. Rigid body dynamics

Vehicle dynamics is described by Newton–Euler equations of motion projected in $\mathbb{F}_B$, namely:

$$(2) \qquad \dot{\mathbf{v}} = -\boldsymbol{\omega} \times \mathbf{v} + \mathbf{F}/m$$

$$(3) \qquad \dot{\boldsymbol{\omega}} = \boldsymbol{J}^{-1}\left[-\boldsymbol{\omega} \times (\boldsymbol{J}\,\boldsymbol{\omega}) + \mathbf{M}\right]$$

where $\boldsymbol{v} = [u,\, v,\, w]^T$ is the linear velocity, $\boldsymbol{\omega} = [p,\, q,\, r]^T$ is the angular velocity,

$$(4) \qquad \boldsymbol{J} = \begin{bmatrix} J_{xx} & -J_{xy} & -J_{xz} \\ -J_{xy} & J_{yy} & -J_{yz} \\ -J_{xz} & -J_{yz} & J_{zz} \end{bmatrix}$$

is the inertia tensor about CG with respect to $\mathcal{F}_B$, and m is the total mass of the rotorcraft. For the aim of the present analysis, it is assumed that both $\boldsymbol{J}$ and m are constant. $\mathbf{F} = [F_x,\, F_y,\, F_z]^T$ and $\mathbf{M} = [M_x,\, M_y,\, M_z]^T$ are the external force and moment vectors, respectively.

The external force acting on the rotorcraft is made of gravity, $\boldsymbol{F}^{(g)}$, and aerodynamic, $\boldsymbol{F}^{(a)}$, contributions. Taking into account Eq. (1), the gravity force vector expressed in the body frame is

$$(5) \qquad \boldsymbol{F}^{(g)} = \boldsymbol{R}(\boldsymbol{\alpha}) \begin{bmatrix} 0 \\ 0 \\ m\,g \end{bmatrix} = m\,g \begin{bmatrix} -\sin\theta \\ \sin\phi\,\cos\theta \\ \cos\phi\,\cos\theta \end{bmatrix}$$

where g is the gravitational acceleration, described by means of WGS84 Taylor series model.[25]

Rotorcraft attitude kinematics, which relates the generalized velocity $\dot{\boldsymbol{\alpha}}$ and the angular velocity $\boldsymbol{\omega}$ is given by:[12]

$$\text{(6)} \quad \dot{\boldsymbol{\alpha}} = \begin{bmatrix} 1 & \sin\phi\tan\theta & \cos\phi\tan\theta \\ 0 & \cos\phi & -\sin\phi \\ 0 & \sin\phi/\cos\theta & \cos\phi/\cos\theta \end{bmatrix} \boldsymbol{\omega}$$

while the position of the helicopter $\boldsymbol{p}_E = [x_E,\, y_E,\, z_E]^T$, with components expressed in the inertial frame $\mathcal{F}_E$, is obtained from the equation:

$$\text{(7)} \quad \dot{\boldsymbol{p}}_E = \boldsymbol{R}(\boldsymbol{\alpha})^T \boldsymbol{v}$$

3.3. Aerodynamic forces and moments

The characterization of the aerodynamic forces, $\boldsymbol{F}^{(a)} = [X,\, Y,\, Z]^T$, and moments, $\boldsymbol{M}^{(a)} = [L,\, M,\, N]^T$, is performed on the basis of the model detailed in,[24] whose nomenclature is adopted in the present framework. A conventional single MR helicopter with teetering configuration and counterclockwise rotation is considered. Contributions are provided by helicopter main rotor (MR), tail rotor (TR), fuselage (F), horizontal stabilizer (HS), upper and lower vertical fins (VF1 and VF2), main rotor hub (MRH), and parachute canopy (PC). Air parameters are calculated from the International Standard Atmosphere (ISA) model as a function of rotorcraft altitude.[26]

3.3.1. MR and TR modeling

The following considerations are made on MR model: a) rotor blades are rigid in bending and torsion; b) flapping angles are small and the analysis follows the simple strip theory;[27] c) the effects of the aircraft motion on the blade flapping are limited to those related to the angular accelerations $\dot{p}$ and $\dot{q}$, the angular rates p and q, and the normal acceleration component $\dot{w}$; d) blade flow stall is disregarded; e) rotor inflow is uniform and no inflow dynamics is modeled; f) main rotor blade flapping is approximated by the first harmonic terms with time–varying coefficients, that is

$$\text{(8)} \quad \beta(t) = a_0 - a_1 \cos\xi - b_1 \sin\xi$$

where a_0 is treated as a preset constant (coning angle) and ξ is blade azimuth. Coefficients $a_1(t)$ and $b_1(t)$ respectively represent the longitudinal and the lateral tilt of the rotor tip–path plane, obtained as solutions to the equations in Appendix C of[24] with null hinge offset ratio, $\epsilon = 0$, flapping spring constant, $K_\beta = 0$, and pitch–flap coupling ratio, $\tan\delta_3 = 0$. Finally, MR shaft is aligned with $\boldsymbol{z}_B$.

The tail rotor is modeled according to a teetering configuration, without cyclic pitch. Provided that the flapping frequency is typically much higher than that of the MR system, the TR tip–path plane dynamics is neglected, no flapping spring constant is considered, but the pitch–flap coupling ratio, δ_{3TR}, is characterized by a non–null value (see Appendix D in[24]).

Differently to some of the assumptions provided in,[24] the blades of both MR and TR are characterized by cambered airfoils with lift–curve slope $a < 2\pi$ 1/rad and zero–lift angle of attack $\alpha_0 \neq 0$. The rotor blade profile drag coefficient, C_d, is calculated as

$$\text{(9)} \quad C_d = 0.008 + 0.3\left(\frac{6\,C_T}{\sigma\,a}\right)^2 + \Delta C_d$$

where C_T is rotor thrust coefficient, σ is rotor solidity, and ΔC_d is the extra drag coefficient determined by flow compressibility effects. Let M_{90} be the Mach number evaluated at the tip of the advancing blade, where $\xi = 90$ deg. In order to estimate the extra drag, the approximate model proposed by Prouty and described in[27] is adopted, where

$$\text{(10)} \quad \Delta C_d(M_{90}) = \begin{cases} 12.5\,(M_{90} - M_{dr})^3 & \text{for } M_{90} \geq M_{dr} \\ 0 & \text{otherwise} \end{cases}$$

and $M_{dr} = 0.74$ is the drag–rise Mach number. With respect to the characterization of rotors inflow, a number of non–ideal effects are considered, based on the approach in,[27] for the characterization of forces and moments. A constant tip–loss factor $B < 1$ is adopted to account for blade tip losses. Other non ideal effects, including nonuniform inflow, wake swirl and contraction, and blades interference are accounted for by an induced power factor k_i, differently estimated for both MR and TR, which is assumed to be a constant. In–ground effect is provided by the model in[28] and the inflow iterative scheme is solved according to Halley's method with damping coefficient equal to 0.01.[29]

Cockpit/RC control of MR is provided by pilot commands in terms of lateral cyclic δ_a, longitudinal cyclic δ_e, and collective δ_c. All commands are expressed in terms of non–dimensional variables, such that $\delta_a \in [-1,\, +1]$ (positive direction: right to generate $L > 0$), $\delta_e \in [-1,\, +1]$ (positive direction: aft to generate $M > 0$), and $\delta_c \in [-1,\, +1]$ (positive direction: up to generate $Z < 0$). Control of the tail rotor by onboard pilot is performed by pedals command, expressed as $\delta_p \in [-1,\, +1]$ (positive direction: right pedal forward to generate $N > 0$). The transformation of pilot commands into blades pitch is provided by a set of low–order polynomial functions, $A_{1s} = C_1(\delta_a)$, $B_{1s} = C_2(\delta_e)$, $\theta_0 = C_3(\delta_c)$, and $\theta_{0TR} = C_4(\delta_p)$, provided by the manufacturer. A_{1s} and B_{1s} respectively represent the lateral and the longitudinal cyclic pitch angle measured from MR hub plane in

$\mathcal{F}_B$. Rotor blades are modeled with a linear twist, such that θ_0 is the blade collective pitch ideally extrapolated to rotor center and θ_{tw} is the total blade twist angle (tip minus root pitch angle). No twist characterizes TR blades, where collective pitch is equal to θ_{0TR}. The functions C_1, C_2, C_3, and C_4, provided by the manufacturer, relate pilot commands to blade pitch and account for the kinematic chain layout.

A rotational degree of freedom is provided to the powerplant made of free turbine, MR, and TR transmissions. In particular, the MR and TR rotational speeds vary according to the current torque requirements and the engine power available. Changes in speed cause the free turbine rpm governor to vary the fuel flow to the engine to change the available power and maintain the desired angular rate. The dynamic model for this degree of freedom is found in.[24] For the sake of brevity, details are not provided in the present paper. Modeling parameters in terms of maximum available power, engine dynamics, specific fuel consumption, and mechanical transmission efficiency are provided by the manufacturer.

3.3.2. Fuselage, empennages, and miscellaneous components

In calculating the fuselage forces and moments, it is assumed that the longitudinal forces and moments are dependent on fuselage angle of attack, and the lateral forces and moments are dependent on angle of sideslip. The exception is the drag force, which is assumed to have a contribution from both angle of attack and sideslip. The modeling is based on a low–angle and a high–angle representation of forces and moments, according to Appendix F in.[24] Phasing between the two approximations is performed by means of cubic spline interpolation, with improved performance with respect to the proposed linear transition. Main fuselage parameters are listed in Appendix 1.

The modeling of the two vertical empennages and the horizontal stabilizer also follows the approach in.[24] The aerodynamics of MR hub and parachute pod is assessed with the equivalent flat plate area model. As an example, the force vector generated by MRH is:

$$(11)\quad \boldsymbol{F}_{MRH} = -\frac{1}{2}\,\rho \begin{bmatrix} A_{xMRH}\,|u_{MRH}|\,u_{MRH} \\ A_{yMRH}\,|v_{MRH}|\,v_{MRH} \\ A_{zMRH}\,|w_{MRH}|\,w_{MRH} \end{bmatrix}$$

where u_{MRH}, v_{MRH}, and w_{MRH} are the velocities, relative to the air mass, of the main rotor hub and include the contribution of MR downwash according to.[30] A_{xMRH}, A_{yMRH}, and A_{zMRH} are the equivalent flat plate drag areas respectively orthogonal to $\boldsymbol{x}_B$, $\boldsymbol{y}_B$, and $\boldsymbol{z}_B$. The moment generated by $\boldsymbol{F}_{MRH}$ about the center of gravity is given by $\boldsymbol{M}_{MRH} = \boldsymbol{d}_{MRH} \times \boldsymbol{F}_{MRH}$, where

$$(12)\quad \boldsymbol{d}_{MRH} = \begin{bmatrix} STA_{CG} - STA_{MRH} \\ BL_{MRH} - BL_{CG} \\ WL_{CG} - WL_{MRH} \end{bmatrix}$$

is the vector directed from CG to the MRH position, assumed to be coincident with its center of pressure, with constant components expressed in $\mathcal{F}_B$.

4. TRIM AND STABILITY ANALYSIS

The nonlinear model described in Section 3, characterized by the data listed in Appendix 1, is implemented in a Matlab/Simulink environment, where differential equations are solved by Dormand–Prince ode8 method with a frequency of 1000 Hz.[31] In what follows, 1) the trim conditions are determined for different cruise speeds, 2) a linearization procedure is then applied to the complete model about the equilibria, and 3) an open–loop dynamic analysis is performed to investigate the helicopter control and stability properties.

4.1. Trim analysis

The helicopter model is numerically trimmed in straight–and–level flight at $h = 50$ m in standard atmospheric conditions. Different values of forward speed are considered, ranging from 0 km/h (hover) to 180 km/h (approximately the never–exceed speed), with steps of 5 km/h. For the sake of brevity, the results of both the static and the following dynamic analysis are summarized only for the hovering condition, for which dedicated flight tests were performed for validation purposes.

Table 1: Trim analysis for the hovering flight.

Parameter	Symbol	Value	Units	Est. error $\lvert\cdot\rvert$
Main Rotor				
Long. first–harmonic flapping coeff.	a_1	2.92	deg	N/A
Lat. first–harmonic flapping coeff.	b_1	-1.10	deg	N/A
Induced speed	v_i	7.79	m/s	N/A
Aerodynamic torque	Q	1 579.5	Nm	3.1%
Tail Rotor				
Long. first–harmonic flapping coeff.	a_{1TR}	0.24	deg	N/A
Lat. first–harmonic flapping coeff.	b_{1TR}	-0.24	deg	N/A
Induced speed	v_{iTR}	11.64	m/s	N/A
Aerodynamic torque	Q_{TR}	26.1	Nm	4.4%
Fuselage				
Roll angle	ϕ	-2	deg	17.6%
Pitch angle	θ	-1.96	deg	6.7%
Control Pitch Angles				
MR lat. cyclic pitch	A_{1_s}	-1.10	deg	4.8%
MR lon. cyclic pitch	B_{1_s}	-2.91	deg	42.0%
MR collective pitch	θ_0	12.62	deg	2.1%
TR collective pitch	θ_{0TR}	8.28	deg	2.1%

The main results of the trim analysis for the hovering condition are given in Table 1 and compared to the data available from flight tests, performed with the same vehicle configuration (deviations with respect to measured data are reported in terms of absolute value of percentage errors). To this end, the Zefhir helicopter was equipped with a set of sensors including: a) potentiometers for cockpit commands acquisition and blade pitch measurement, b) torquemeters for MR and TR torque analysis, c) an attitude and heading reference system (AHRS) providing rigid body attitude, angular rate, acceleration, speed, and position information.

According to Table 1, a good agreement is found between predicted and measured values, showing the validity of the modeling approach. Major difference characterizes the value of longitudinal cyclic pitch, with an error 42%. In this respect, it must be noted that a certain degree of uncertainty characterizes the knowledge of CG position (especially the STA_{CG} parameter) in the actual flight configuration, being estimated by means of CAD analysis and suspension techniques. Uncertainty also characterizes the aerodynamics of the fuselage, especially in the case of hovering and low–speed forward flight, where MR wake envelops a good part of the fuselage. For the aim of the present analysis, the model adopted for both MR inflow and the fuselage aerodynamics necessarily represents a compromise solution, which allows for satisfactory accuracy in terms of dynamic characterization of the rotorcraft, without the cost of more complicate aerodynamic models.

The match expected at hover between the MR cyclic pitch angles and the flapping coefficients, namely $A_{1s} = b_1$ and $B_{1s} = -a_1$, holds almost exactly in Table 1. Slight differences occur for the simulated hover condition, which is actually obtained by flying the helicopter at a stabilized residual forward speed of 0.1 m/s. With respect to the experimental campaign, effective environmental conditions were also monitored, provided the helicopter was maintained in upwind hover, while estimating a maximum wind speed of 20 km/h.

4.2. Dynamic analysis

Consider the helicopter equations of motion introduced in Section 3 and detailed in.[24] In nonlinear form, it is

$$\dot{\boldsymbol{x}} = \boldsymbol{f}\left(\boldsymbol{x}, \boldsymbol{u}, t\right) \tag{13}$$

provided x is the rigid–body state vector, namely

$$\boldsymbol{x} = [u,\, w,\, q,\, \theta,\, v,\, p,\, \phi,\, r]^T \tag{14}$$

while the time evolution of x_E, y_E, z_E, and ψ is not accounted in the framework of system linearization about a forward flight condition. The control vector $\boldsymbol{u}$ has four components, expressed in terms of pilot commands as:

$$\boldsymbol{u} = [\delta_c,\, \delta_e,\, \delta_a,\, \delta_p]^T \tag{15}$$

Using small perturbation theory,[28] it is assumed that the helicopter behavior is described as a perturbation from the generic equilibrium condition, $\boldsymbol{x}_e = [U_e, W_e, Q_e, \Theta_e, V_e, P_e, \Phi_e, R_e]^T$ and $\boldsymbol{u}_e = [U_{1e}, U_{2e}, U_{3e}, U_{4e},]^T$, written in the form $\boldsymbol{x} = \boldsymbol{x}_e + \delta\boldsymbol{x}$ and $\boldsymbol{u} = \boldsymbol{u}_e + \delta\boldsymbol{u}$. By following the approach and the nomenclature of,[28] given the trim conditions obtained in Section 4.1, the model in Eq. (13) is linearized at all considered speeds in order to obtain the system and input matrices

$$\boldsymbol{A} = \left(\frac{\partial \boldsymbol{f}}{\partial \boldsymbol{x}}\right)_{\boldsymbol{x}_e,\, \boldsymbol{u}_e}, \quad \boldsymbol{B} = \left(\frac{\partial \boldsymbol{f}}{\partial \boldsymbol{u}}\right)_{\boldsymbol{x}_e,\, \boldsymbol{u}_e} \tag{16}$$

as a function of aerodynamic derivatives. The latter are estimated by numerical differencing in Matlab/Simulink environment.[28] To this aim, the aerodynamic forces and moments are positively perturbed by each of the state and input vector components in turn with amplitude equal to 0.02 (respectively intended in terms of m/s for u, v, w, rad/s for p, q, r, rad for ϕ, θ, and non–dimensional units for control inputs). State and control derivatives are written in the form:

$$X_u = \frac{1}{m}\,\frac{\partial X}{\partial u} \tag{17}$$

and

$$L'_p = \frac{J_{zz}}{J_{xx}\,J_{zz} - J_{xz}^2}\,\frac{\partial L}{\partial p} + \frac{J_{xz}}{J_{xx}\,J_{zz} - J_{xz}^2}\,\frac{\partial N}{\partial p} \tag{18}$$

$$N'_r = \frac{J_{xz}}{J_{xx}\,J_{zz} - J_{xz}^2}\,\frac{\partial L}{\partial r} + \frac{J_{xx}}{J_{xx}\,J_{zz} - J_{xz}^2}\,\frac{\partial N}{\partial r} \tag{19}$$

A total of 36 stability derivatives and 24 control derivatives are determined in the standard 6DOF representation for each flight condition. Due to the highly–classified nature of the data involved in an early stage of the aircraft development, only one sample derivative is analyzed in the present paper at hover. A qualitative discussion about the behavior of the most significant derivatives is provided in what follows.

The effect of linear velocity on aerodynamic forces is principally taken into account by X_u, Y_v, and Z_w. The force damping derivatives $X_u < 0$ and $Y_v <$, that respectively reflect the drag and side force on the rotor–fuselage combination, steadily increase in absolute value and are practically linear with speed beyond 50 km/h. At low speed, the effect of disc tilt following perturbations in u and v becomes predominant. Similar considerations hold for the heave damping derivative Z_w, which is mostly influenced by the fuselage and horizontal empennage in high–speed flight. At low speed, the MR tends to dominate Z_w through a reduction of

C_T, following a vertical speed perturbation. In order to validate the numerical linearization procedure, a comparison is performed with the analytical results obtained for the stability and control derivatives according to formulas available in the literature. As an example, the MR contribution only to Z_w can be analytically estimated as[28]

$$Z_w = -\frac{\rho\,(\Omega\,R)\,\pi\,R^2}{m}\frac{\partial C_T}{\partial \mu_z} \tag{20}$$

where $\mu_z = w/\,(\Omega\,R)$ is MR climb ratio and

$$\frac{\partial C_T}{\partial \mu_z} \approx \frac{2\,a\,\sigma\,|\lambda|}{16\,|\lambda| + a\,\sigma} \tag{21}$$

Based on the data in Appendix 1 and Table 1, it is $\lambda = -0.0371$ at hover, such that $\partial C_T/\partial \mu_z \approx 0.018$. It follows $Z_w \approx -0.317$ 1/s, which is close to the value numerically obtained in the same condition for the full helicopter, namely -0.345 1/s. In such a case, the estimation error obtained according to literature results is -8.1%, provided that fuselage and appendages contribution is disregarded.

The so–called speed stability effect is observed in $M_u > 0$ and $L'_v < 0$, the latter showing a practically linear behavior with speed. $M_w > 0$ is representative of the incidence static stability effect, which increases non–monotonically with speed and approximately tracks M_u, being influenced by MR inflow on helicopter components. Finally, the derivative $N'_v > 0$ accounts for the weathercock effect by means of TR and vertical fins (stabilizing with speed) and the fuselage (destabilizing).

The damping derivatives $L'_p < 0$, $M_q < 0$, and $N'_r < 0$ reflect short–term, small and moderate–amplitude, handling characteristics. If, on the one hand, L'_p and M_q principally account for MR flapping motion in the presence of roll and pitch rate perturbations, N'_r is dominated by loads on the TR and the vertical fins, with a stronger yaw–damping effect at high forward speeds.

Given the stability and control derivatives obtained above, the complete system and input matrices $\boldsymbol{A}$ and $\boldsymbol{B}$ are generated according to the structure provided on page 277 in.[28] Note that, with the idea of designing the closed–loop control systems, the input matrix $\boldsymbol{B}$ is configured for application to the non–dimensional pilot commands. The formulation in terms of blade pitch control angles is however possible by means of functions C_1, C_2, C_3, and C_4 introduced in Section 3.3.1.

For the aim of the present work, however, the results of a decoupled analysis are first discussed. Based on the approximate separation between the longitudinal and the lateral–directional dynamics, the decoupled representation is available from,[28] where input matrices are applied to blade pitch control angles. The longitudinal dynamics is described by the forced system:

$$\begin{aligned}\frac{d}{dt}\begin{bmatrix} u \\ w \\ q \\ \theta \end{bmatrix} &= \underbrace{\begin{bmatrix} X_u & X_w & X_q - W_e & -g\,\cos\Theta_e \\ Z_u & Z_w & Z_q + U_e & -g\,\sin\Theta_e \\ M_u & M_w & M_q & 0 \\ 0 & 0 & 1 & 0 \end{bmatrix}}_{\boldsymbol{A}_{lon}} \begin{bmatrix} u \\ w \\ q \\ \theta \end{bmatrix} \\ &+ \underbrace{\begin{bmatrix} X_{\theta_0} & X_{B_{1s}} \\ Z_{\theta_0} & Z_{B_{1s}} \\ M_{\theta_0} & M_{B_{1s}} \\ 0 & 0 \end{bmatrix}}_{\boldsymbol{B}_{lon}} \begin{bmatrix} \theta_0 \\ B_{1s} \end{bmatrix}\end{aligned} \tag{22}$$

A pair of complex–conjugate poles is determined from $\boldsymbol{A}_{lon}$, which is related to an unstable phugoid mode with natural frequency ω_{ph} and time constant τ_{ph} (calculated as the reciprocal of the real part of the poles, in its absolute value). Two real stable modes are also evaluated, namely the heave and pitch subsidence. The first pole, identified by $p_{hv} < 0$, is practically determined by the vertical damping derivative Z_w discussed above. The second pole, $p_{ps} < 0$, accounts for the fundamental contribution of both Z_w and M_q and is characterized by a time constant approximately estimated as $\tau_{ps} \approx -1/\,(Z_w + M_q)$.[28] The decoupled lateral–directional dynamics is described by the system:

$$\begin{aligned}\frac{d}{dt}\begin{bmatrix} v \\ p \\ r \\ \phi \end{bmatrix} &= \underbrace{\begin{bmatrix} Y_v & Y_p + W_e & Y_r - U_e & g\,\cos\Phi_e\,\cos\Theta_e \\ L'_v & L'_p & L'_r & 0 \\ N'_v & N'_p & N'_r & 0 \\ 0 & 1 & \cos\Phi_e\,\tan\Theta_e & 0 \end{bmatrix}}_{\boldsymbol{A}_{lat}} \begin{bmatrix} v \\ p \\ r \\ \phi \end{bmatrix} \\ &+ \underbrace{\begin{bmatrix} Y_{A_{1s}} & Y_{\theta_{0TR}} \\ L'_{A_{1s}} & L'_{\theta_{0TR}} \\ N'_{A_{1s}} & N'_{\theta_{0TR}} \\ 0 & 0 \end{bmatrix}}_{\boldsymbol{B}_{lat}} \begin{bmatrix} A_{1s} \\ \theta_{0TR} \end{bmatrix}\end{aligned} \tag{23}$$

A pair of complex–conjugate poles is derived from $\boldsymbol{A}_{lat}$ with natural frequency ω_{dr}. Such poles characterize the dutch–roll mode, which is unstable but slowly develops with a time constant τ_{dr}. The roll subsidence mode, mostly determined by the damping derivative L'_p, is related to the real pole $p_{roll} < 0$. The spiral subsidence mode at hover is stable, $p_{spiral} < 0$, and dampens with a time constant τ_{spiral}.

The analysis of the coupled representation obtained in state matrix $\boldsymbol{A}$ is also considered and obtained poles are marked by superscript 'c'. A comparison with the corresponding values derived through the decoupled analysis is provided, where possible. Two real poles are first extracted. The roll subsidence effect is recognized in the first pole, $p_1 = 0.85 \cdot p_{roll}$, provided $p_1 \approx L'_p$. The same consideration holds for the vertical damping mode, identified by $p_8^{(c)} \approx p_{hv} \approx Z_w$. Three pair of complex–conjugate poles complete the analysis. The first pair, $p_{2,3}^{(c)}$, is stable with real part proportional to $M_q + Z_w$. It is representative of a damped oscillation, with natural frequency $\omega_{py}^{(c)}$ and time constant $\tau_{py}^{(c)}$, determined by the coupling of the pitch and yaw subsidence modes. The second pair, $p_{4,5}^{(c)}$, characterizes the unstable phugoid mode, which develops with a time constant $\tau_{ph}^{(c)} = 0.75 \cdot \tau_{ph}$ and shows a natural frequency $\omega_{ph}^{(c)} = 1.38 \cdot \omega_{ph}$. The last pair of complex poles, $p_{6,7}$ is related to the dutch roll motion, which is unstable and develops with natural frequency $\omega_{dr}^{(c)} = 0.92 \cdot \omega_{dr}$ and time constant $\tau_{dr}^{(c)} = 1.07 \cdot \tau_{dr}$.

4.3. Model validation

In Section 4 a comparison is provided between simulated and measured variables regarding the static characterization of the hovering condition. In what follows, predicted dynamic properties about the same equilibrium are validated through experimental identification methods.[33]

To this end, flight data are collected and eventually filtered after performing frequency sweep maneuvers about the hover, according to the approach described in.[34] The frequency response for each selected input–output pair is then identified during an optimization process driven by the difference between the computed and the predicted frequency responses. The fidelity of the model is finally established using time domain verification, according to which the time response identified by the model is compared to the response recorded during flight tests.

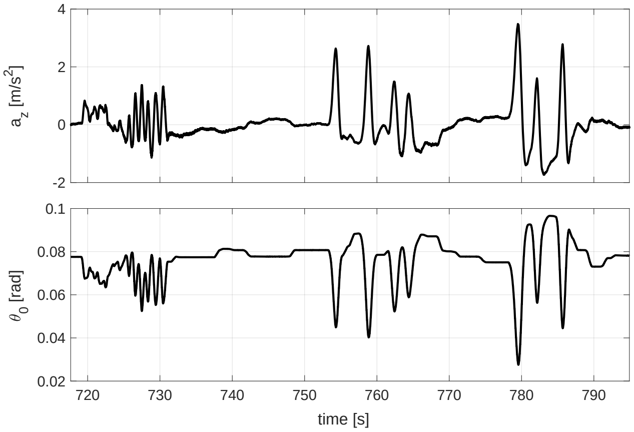

Figure 5: The input–output measured data used for heave subsidence mode characterization near hover (detail).

Different maneuvers and data pairs are considered for the identification of transfer functions, such as $p(s)/A_{1s}(s)$ and $q(s)/B_{1s}(s)$, with the aim to validate the predicted dynamic information. For the sake of brevity, the adopted procedure is detailed in what follows only for the characterization of the heave subsidence mode, whose dominant derivative Z_w was discussed above. In particular, the first input–output data pair to be analyzed describes the effect of MR collective pitch angle θ_0 to the vertical acceleration, $a_z = \dot{w}$, expressed in body–fixed axis. A detail of the data taken into account for the identification procedure are reported in Figure 5. The predicted transfer function as obtained from the state–space representation in Eq. (22) is:

$$\left.\frac{a_z\,(s)}{\theta_0\,(s)}\right|_{mdl} = \frac{Z_{\theta_0}\, s(s-z_1)(s-z_2)(s-z_3)}{(s-p_{hv})\,(s-p_{ps})\left(s^2 - 2/\tau_{ph}\, s + \omega_{ph}^2\right)} \tag{24}$$

where a set of 4 system zeros is determined. The first one is located at the origin, $z_1 = 0.9983\, p_{ps}$ is real negative, and z_2,z_3 are a complex–conjugate pair such that $z_2\, z_3 = 1.008\, \omega_{ph}^2$ and $z_2 + z_3 = 1.059 \cdot 2/\tau_{ph}$. The heave subsidence mode evidently dominates the motion along $\boldsymbol{z}_B$, provided that almost perfect pole–zero cancellation characterizes the terms depicted in gray color. Hence, it follows:

$$\left.\frac{a_z\,(s)}{\theta_0\,(s)}\right|_{mdl} \approx \frac{Z_{\theta_0}\, s}{s - p_{hv}} \tag{25}$$

Identification is performed by using a Prediction Error Minimization (PEM) method focused on simulation,[35] provided the transfer function in Eq. (24) is assumed as the initial guess model. The identified transfer function is:

$$\begin{aligned} \left.\frac{a_z\,(s)}{\theta_0\,(s)}\right|_{id} &= \frac{0.9964\, Z_{\theta_0} (s-\pi_1)\,(s-\pi_2)}{(s-1.0421\, p_{hv})\,(s-0.9912\,\pi_2)} \\ &\quad \cdot \frac{\left(s^2+\pi_3\, s+\pi_4\right)}{\left(s^2+1.0090\,\pi_3\, s+0.9964\,\pi_4\right)} \\ &\approx \frac{0.9964\, Z_{\theta_0}\, s}{(s-1.0421\, p_{hv})} \end{aligned} \tag{26}$$

where pole–zero cancellation can be evidently performed for the gray terms. It must be noted that $\pi_1 \approx 0$, such that the zero in the origin is also recovered. The estimation error between model–predicted and identified parameters is provided in the second line of Eq. (26), where the updated values of $|Z_{\theta_0}|$ and $|p_{hv}|$ respectively result to be 0.36% smaller and 4.21% bigger than the model–based ones in Eq. (25). A sample comparison between measured and refined–simulation data, after heave subsidence mode characterization, is finally provided in Figure 6 for the acceleration.

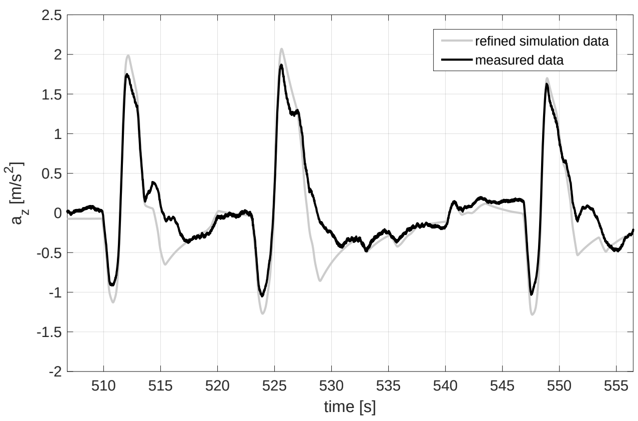

Figure 6: Measured and simulated data after heave subsidence mode characterization at hover (detail).

Encouraging results are indeed obtained for other input–output pairs, thus validating the modeling approach. In all cases, in fact, very good agreement is found between the dynamic properties obtained through numerical simulation and identification techniques.

5. CONTROL SYSTEM DESIGN AND TEST

In what follows, the control system design phase is described, based on the mathematical model in Section 3 and the open–loop stability analysis performed in Section 4. The closed–loop system is first analyzed by Model–In–the–Loop (MIL) simulations, where control gains are preliminary sized. HIL tests are then performed to refine the control action and to validate the software/hardware setup.[36]

5.1. Model–In–the–Loop validation

Pilot commands, here named $\delta_a^{(pilot)}$, $\delta_e^{(pilot)}$, $\delta_c^{(pilot)}$, and $\delta_p^{(pilot)}$ are an input to the control system and follow the same convention described in Section 3.3.1. According to the given requirements, no closed–loop control is designed for MR collective pitch, such that $\delta_c \equiv \delta_c^{(pilot)}$.

In the framework of control systems design, mathematical models for the selected AHRS and actuators are also developed. Modeling parameters in terms of accuracy and performance are obtained from both datasheet and dedicate experiments performed through laboratory facilities.

The first controller is adopted to stabilize the yaw motion by the actuation of TR collective pitch angle θ_{0TR} and the closed-loop feedback of yaw rate r. Let $e_r = \xi_r \, \delta_p^{(pilot)} - r$ be the error between the desired and the measured angular rate, provided that $\xi_r > 0$ is a prescribed constant which transforms the non–dimensional command provided by the remote pilot into the desired yaw rate. The control scheme is described by the equation:

$$\delta_p = k_p^{(r)} \, e_r + k_i^{(r)} \int_0^t e_r(s) \, ds \tag{27}$$

where $k_p^{(r)} > 0$ and $k_i^{(r)} > 0$ are control gains respectively providing proportional and integral contributions related to the error signal $e_r(t)$.

The second controller is used to stabilize the attitude of the helicopter in terms of roll and pitch angles by the actuation of lateral and longitudinal cyclic control angles, respectively. With respect to the roll angle stabilization, it is:

$$\delta_a = k_p^{(\phi)} \, e_\phi + k_i^{(\phi)} \int_0^t e_\phi(s) \, ds + k_d^{(\phi)} \, p \tag{28}$$

where $k_p^{(\phi)} > 0$ and $k_i^{(\phi)} > 0$. A derivative–like contribution is also provided by the direct feedback of roll rate p through the gain $k_d^{(\phi)} < 0$. The error between the desired and the measured roll angle is calculated as $e_\phi = \xi_\phi \, \delta_a^{(pilot)} - \phi$, where $\xi_\phi > 0$ is a prescribed constant. The controller structure for the stabilization of pitch angle follows the same approach, namely:

$$\delta_e = k_p^{(\theta)} \, e_\theta + k_i^{(\theta)} \int_0^t e_\theta(s) \, ds + k_d^{(\theta)} \, q \tag{29}$$

where $k_p^{(\theta)} > 0$, $k_i^{(\theta)} > 0$, and $k_d^{(\theta)} < 0$. The error between the desired and the measured pitch angle is $e_\theta = \xi_\theta \, \delta_e^{(pilot)} - \theta$, where $\xi_\theta > 0$.

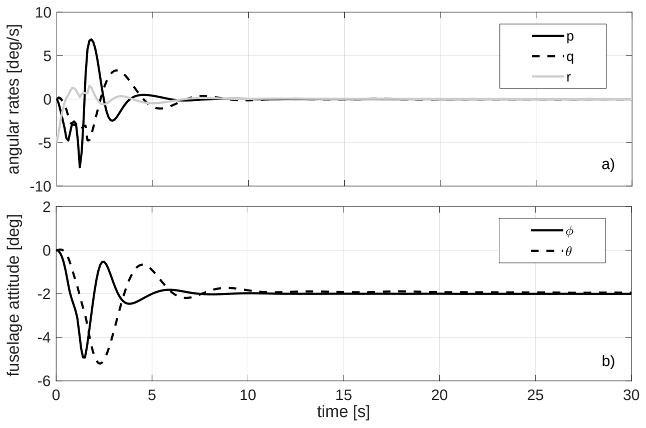

Figure 7: MIL stabilization of attitude variables.

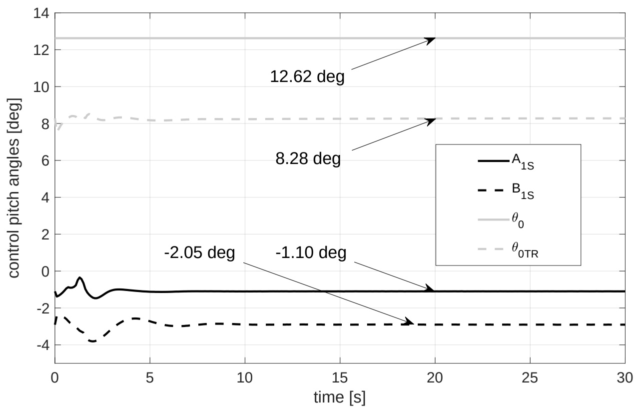

Figure 8: MIL stabilization of control pitch angles to the hovering configuration.

In Figures 7 and 8 the results of a sample maneuver are reported. The simulation is started at $h = 50$ m with null attitude of the helicopter ($\phi_0 = \theta_0 = \psi_0 = 0$ deg) and an initial angular rate about the yaw axis, such that $p_0 = q_0 = 0$ deg/s and $r_0 = -5$ deg/s. The MR collective pitch angle is kept constant and equal to the value obtained in Table 1 for the hovering condition, namely $\theta_0 = 12.62$ deg, corresponding to $\delta_c^{(pilot)} = 0.495$. Let $\xi_r = 40 \cdot \pi/180$ rad/s, $\xi_\phi = 25 \cdot \pi/180$ rad, and $\xi_\theta = 12 \cdot \pi/180$ rad. The input values for the controllers are $\delta_p^{(pilot)} = 0$, $\delta_a^{(pilot)} = -0.08$, and $\delta_e^{(pilot)} = -0.163$, which respectively provide the desired values $\phi = -2$ deg, $\theta = -1.96$, and $r = 0$ deg/s required for hovering. In Figure 7 the state variables representing fuselage attitude are plotted as a function of time, showing the stabilizing effect of implemented controllers. The corresponding control pitch angles are depicted in Figure 8, where the hover trim variables reported in Table 1 are retrieved. Given the highly–classified nature of the data involved during the dronization process, the adopted first–guess controller gains are omitted.

5.2. Hardware–In–the–Loop validation

The simulation setup described above is deployed to a HIL laboratory facility according to the scheme depicted in Figure 9. Involved components are set up as follows:

- The software developed in Matlab/Simulink for the mathematical modeling of helicopter dynamics and AHRS device is automatically coded and deployed to a high–performance Real–Time Target Machine (RTTM) by Simulink Real–Time$^{\text{TM}}$ tools. The solver frequency is set at 20 kHz, while AHRS model data are generated at 100 Hz. Software coding and deployment are performed through a host desktop PC where FlightGear open–source application is used to represent simulation data by a 3D graphical interface.
- The output of RTTM is provided via a dedicated standard industrial bus I/O module by two isolated ports. The first port is used to output the emulated AHRS data. The second port is used to generate repeatable control commands for HIL validation only, as if they were provided by the pilot on the ground.

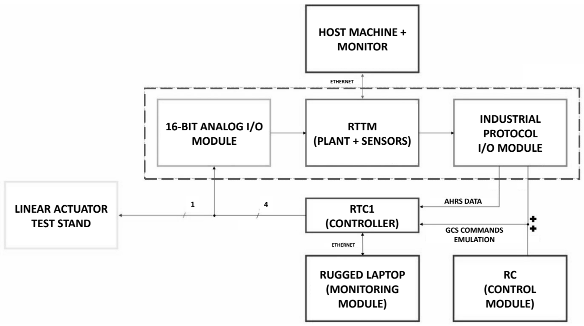

Figure 9: Sketch of HIL simulation setup.

- AHRS data and pilot commands from the RC device are the inputs to the onboard computer. At the time of HIL experiments the RTC2 was already mounted on the helicopter as a pure acquisition device for an extensive campaign of manned flight tests. Hence, laboratory HIL tests were performed by using the RTC1 as onboard computer. To emulate the presence of the radio modem, signals from the RC are converted from serial to standard industrial protocol by a microcontroller board equipped with a dedicate conversion shield. The control laws designed in Matlab/Simulink are coded and deployed to the RTC1 through the rugged laptop. The code developed for the onboard computer makes use of proprietary libraries for PID control implementation, acquisition and processing of input signals (including the applicaton of Butterworth filters with order 1 and cut–off frequency of 5 Hz to measured data), and real–time monitoring of selected variables.
- Control signals are acquired through a terminal board by a dedicated I/O module, a 16 bit analog input device selected to close the control loop. An ad hoc test bench is also provided where 1 linear actuator is controlled, in turn, by a voltage signal. Information about the linear motion are acquired and made available to evaluate the performance.

Different maneuvers are performed during HIL simulations in order to validate the control strategy in Section 5.1 and the hardware implementation. For the sake of brevity, only a sample case is reported in what follows. In particular, starting from a hovering condition, a step input $\delta_a^{(pilot)} = 0.08$ is generated via the RTTM in order to reach a desired roll angle of 2 deg, while keeping the other inputs unaltered. In Figures 10 and 11 the results of the maneuver are reported in terms of variation with respect to the hovering variables.

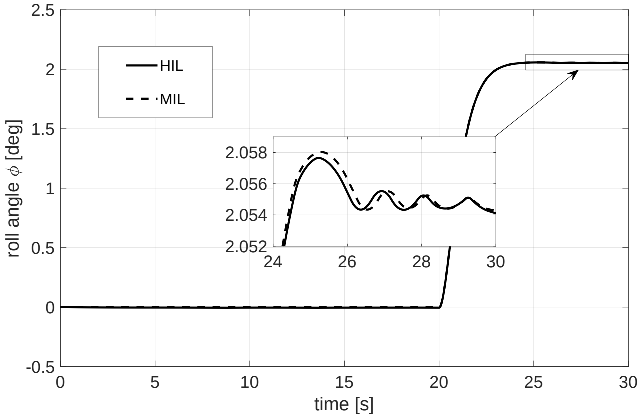

Figure 10: Roll angle stabilization maneuver: comparison between MIL and HIL simulations (roll angle, variation with respect to the hover condition).

It can be noted that, given the same sample maneuver, the error between the HIL and MIL simulations always remains bounded and smaller than 0.001 deg (roll angle) and 0.005 deg/s (roll rate). Also, discretization and quantization effects of signals are investigated, which however do not affect controllers efficacy. This and many other simulation tests validate the quality of the simulation software and the correct implementation of acquisition, actuation, and control system protocols in the presence of real flight hardware in a controlled environment, prior to flight.

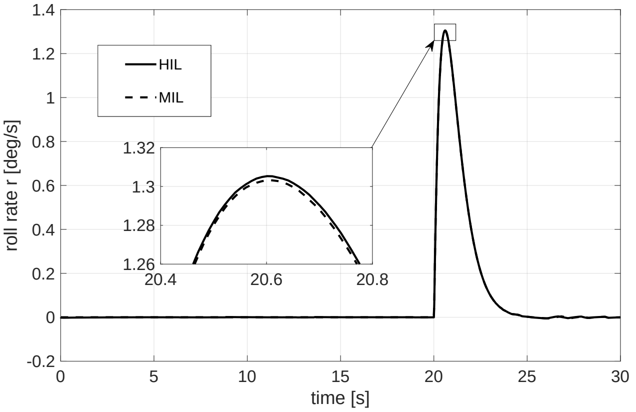

Figure 11: Roll angle stabilization maneuver: comparison between MIL and HIL simulations (roll rate).

6. FLIGHT TESTS WITH THE UNMANNED HELICOPTER

After an extensive campaign of HIL simulations, aiming at the fine–tuning of controller gains and the correct setup of hardware implementation, the helicopter is finally configured for unmanned flight tests and equipped with the ballistic parachute canopy. In order to simulate the presence of pilots on board, sandbags are put on the 2 seats, thus replicating the inertial configuration analyzed in Section 4, except for the presence of the pod. The campaign, performed in June 2018 at the airport of Oristano–Fenosu (Sardinia, Italy) over 4 days, is organized according to the following steps:

1. Step 1. Direct control of onboard actuators by remote pilot commands, such that $\delta_a = \delta_a^{(pilot)}$, $\delta_e = \delta_e^{(pilot)}$, $\delta_c = \delta_c^{(pilot)}$, and $\delta_p = \delta_p^{(pilot)}$. This piloting configuration allows to validate the overall actuation setup and represents a reversion mode in case of AHRS failure (manual mode).

2. Step 2. The controller in Eq. (27) is activated in order to stabilize the yaw rate. Different flight tests are performed and control gains are refined, according to remote pilot preferences, such that $k_p^{(r)}$ and $k_i^{(r)}$ are respectively increased by about 15% and 14% with respect to the first–guess values in Section 5.1.

3. Step 3. Before activating the controllers in Eqs. (28) and (29), an intermediate test is performed in order to evaluate the damping contribution only provided by gains $k_d^{(\phi)}$ and $k_d^{(\theta)}$ to the flying qualities about the roll and the pitch axis, respectively. To this aim, the yaw rate is stabilized as in Step 2, while direct control action of the pilot on lateral and longitudinal cyclic commands is supported by roll and pitch damper controllers, configured as follows:

   (30) $\delta_a = \delta_a^{(pilot)} + k_d^{(\phi)}\, p$

   (31) $\delta_e = \delta_e^{(pilot)} + k_d^{(\theta)}\, q$

   At the end of Step 3, control gains are fine–tuned such that $k_d^{(\phi)}$ and $k_d^{(\theta)}$ are respectively increased by about 2% and 13% with respect to the first–guess values.

4. Step 4. The attitude controllers in Eqs. (28) and (29) are investigated, leaving the pilot direct control on MR collective pitch only. Control gains are corrected such that $k_p^{(\theta)}$ and $k_i^{(\theta)}$ are respectively

increased by 25% and 60% with respect to the precautionary small values proposed in Section 5.1. Finally, $k_p^{(\phi)}$ and $k_i^{(\phi)}$ are left unaltered.

In what follows, some flight data are reported which describe the tests performed after Step 4, with the unmanned system in its definitive mission configuration.

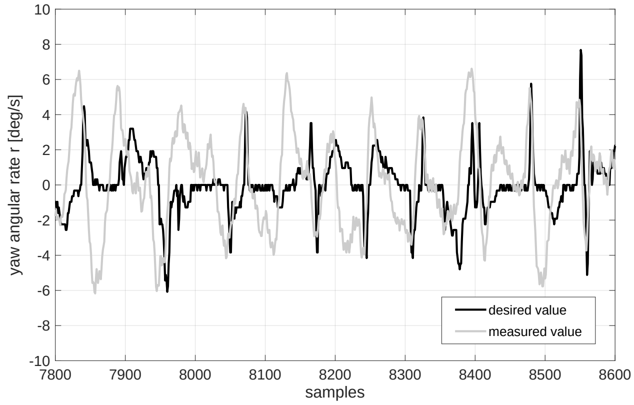

Figure 12: Yaw rate stabilization in a near–hover condition (flight tests, 10 Hz sampling).

As an example, in Figure 12 the commanded value of yaw rate, calculated as $\xi_r\,\delta_p^{(pilot)}$ (black line), is compared to the corresponding value measured by the AHRS (gray line). Data are expressed in deg/s and show the correlation between the desired and the achieved attitude motion while the pilot performs oscillatory yawing maneuvers.

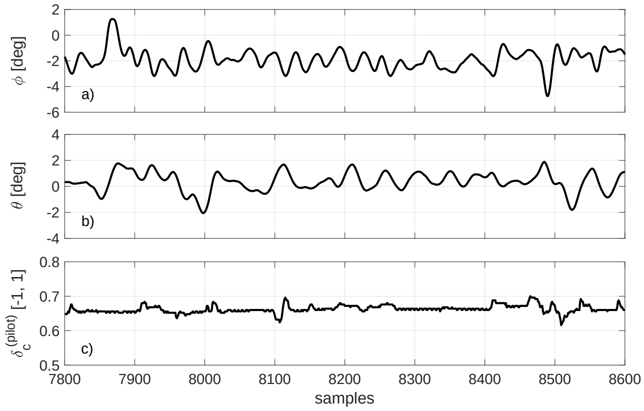

Figure 13: a,b) Attitude stabilization and c) collective pitch command in a near–hover condition (flight tests, 10 Hz sampling).

In Figure 13.a and Figure 13.b the stabilization of roll and pitch angles is also respectively analyzed over the same time period (80 s). In particular, the roll angle oscillates with a standard deviation of 0.78 deg about the mean value of -1.91 deg. Similar considerations hold for the pitch angle, characterized by a standard deviation of 0.74 deg and a mean value of 0.35 deg. If, on the one hand, the roll angle is consistent with the simulation results obtained in Table 1, the pitch angle shows major difference. This is caused by the presence of light tail wind and the fact that the inertial and aerodynamic configuration of the unmanned helicopter differs because of the presence of the parachute pod over the MR hub. The collective command, characterized by a standard deviation of 0.01, remains almost constant and equal to 0.66 (corresponding to 13.67 deg pitch angle).

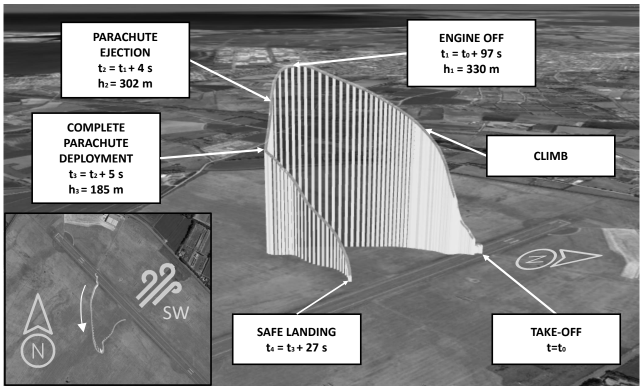

Figure 14: Trajectory followed during the final mission with parachute ejection (Maps Data: Google Earth ©2020 TerraMetrics).

Figure 15: Parachute ejection phases (courtesy of Curti Aerospace Division).

The final experiment, performed on June 22nd, is described by Figure 14, where helicopter trajectory is plotted in the $3D$ environment. Position data are obtained from GPS measurements performed by the AHRS and recorded by the RTC2. After the initial phase required for pre–flight checks and turbine engine warm up, the take–off occurs at time t_0. The climb phase to the height $h_1 = 330$ m is performed in $t_1 - t_0 = 97$ s in the presence of SW wind, with an average vertical speed of about 3.4 m/s. In particular, during the first 40 s the climb rate is stabilized at 2 m/s by pilot's action and then pushed to 4.5 m/s until reaching the maximum height. At time t_1 the flight termination procedure is activated by switching–off the engine and commanding parachute ejection at time $t_2 = t_1 + 4$ s. Complete parachute deployment is performed in about 5 s, at time $t_3 = t_2 + 5$ s (see Figure 15). During the helicopter accelerated free fall the total height loss is $h_3 - h_2 = -146$ m, with an average vertical speed of -16.2 m/s. After $t = t_3$ the rate of descent stabilizes to a practically constant value of 7.5 m/s until the helicopter safely lands at $t_4 = t_3 + 27$ s. The effect of wind is visible in Figure 14, where helicopter trajectory deviates in the North–East direction and stops near the runway at about 285 m from the take–off point.

7. CONCLUSIONS

In the present paper, the complete procedure followed to transform a light helicopter by Curti Aerospace Division into an unmanned rotorcraft was described. By adopting the MBD approach, mission requirements were first set and the design of control system was addressed in terms of software and hardware definition. Particular attention was devoted to the mathematical model of the helicopter and its subsystems, made on the basis of geometric, inertial, and aerodynamic data provided by the manufacturer and later refined by identification techniques.

With the purpose of validating an innovative ballistic parachute rescue system, a closed–loop control system was thus developed in order to allow stable maneuvering in the field of view of a remote pilot. To this end, attitude stabilization algorithms were first tested in a Model–In–the–Loop environment. Then, laboratory experiments allowed for Hardware–In–the–Loop validation of involved equipments and control software deployment on real–time target machines. Dedicated flight tests were performed, proving the effectiveness of the approach and the achievement of the desired closed–loop flying qualities. The final mission successfully showed the feasibility of the proposed termination procedure, allowing for helicopter safe landing in the event of engine failure. The experiment also allowed researchers to focus on the design and experimental validation of technologies at the core of future UAM, envisaging a more efficient, safe, and possibly sustainable exploitation of the vertical dimension.

DECLARATION OF COMPETING INTEREST

The authors declare that they have no known competing financial interests or personal relationships that could have appeared to influence the work reported in this paper.

ACKNOWLEDGEMENTS

The authors wish to express their sincerest gratitude to Hypertech Solution S.r.l., for the effective cooperation that allowed the successful achievement of the goal.

APPENDIX 1. MAIN GEOMETRIC HELICOPTER DATA

Table 2: MR and TR relevant parameters.

Parameter	Symbol	Computer mnemonic	Value	Units
Main Rotor				
MR radius	R_{MR}	ROTOR	3.8	m
MR chord	c_{MR}	CHORD	0.195	m
MR rotational speed	Ω_{MR}	OMEGA	528.5	rpm
MR hinge offset	ε	EPSLN	0	percent/100
MR flapping spring constant	K_β	AKBETA	0	N m/rad
MR tangent of δ_3	K_1	AKONE	0	-
MR solidity	σ_{MR}	SIGMA	0.0327	-
MR hub stationline	STA_H	STAH	2	m
MR hub buttline	BL_H	BLH	0	m
MR hub waterline	WL_H	WLH	2.4	m
Tail Rotor				
TR radius	R_{TR}	RTR	0.57	m
TR chord	c_{TR}	cTR	0.12	m
TR rotational speed	Ω_{TR}	OMTR	3 061.8	rpm
TR tangent of δ_3	K_{1TR}	FKITR	1	-
TR solidity	σ_{TR}	STR	0.0382	-
MR hub stationline	STA_{TR}	STATR	6.4	m
MR hub buttline	BL_{TR}	BLTR	-0.25	m
MR hub waterline	WL_{TR}	WLTR	1.34	m

Table 3: Fuselage, empennages, and miscellaneous components location.

Parameter	Symbol	Computer mnemonic	Value	Units
Fuselage (Fus.)				
Fus. aerodynamic reference point stationline	STA_{RPF}	STARPF	0	m
Fus. aerodynamic reference point buttline	BL_{RPF}	BLRPF	0	m
Fus. aerodynamic reference point waterline	WL_{RPF}	STARPF	0	m
Horizontal stabilizer (HS)				
HS stationline	STA_{HS}	STAHS	6.199	m
HS buttline	BL_{HS}	BLHS	0.435	m
HS waterline	WL_{HS}	WLHS	1.394	m
Upper vertical fin (VF1)				
VF1 stationline	STA_{VF1}	STAVF1	6.1	m
VF1 buttline	BL_{VF1}	BLVF1	0.052	m
VF1 waterline	WL_{VF1}	WLVF1	1.683	m
Lower vertical fin (VF2)				
VF2 stationline	STA_{VF2}	STAVF2	6.069	m
VF2 buttline	BL_{VF2}	BLVF2	0.048	m
VF2 waterline	WL_{VF2}	WLVF2	0.996	m
Main rotor hub (MRH)				
MRH stationline	STA_{MRH}	STAMRH	2	m
MRH buttline	BL_{MRH}	BLMRH	0	m
MRH waterline	WL_{MRH}	WLMRH	2.4	m
Parachute canopy (PC)				
PC stationline	STA_{PC}	STAPC	2	m
PC buttline	BL_{PC}	BLPC	0	m
PC waterline	WL_{PC}	WLPC	2.468	m

References

[1] C. Le Tallec, A. Joulia, M. Harel, A personal plane air transportation system - The PPlane Project, SAE International Journal of Aerospace, Vol. 4, No. 2, 2011, 1281–1292, doi:10.2514/6.2011-6965

[2] J. Hlinka, H. Trefilova, Identification of major safety issues for a futuristic personal plane concept, Aviation, Vol. 18, No. 3, 2014, 120–128, doi: 10.3846/16487788.2014.969880

[3] L.A. Garrow, B.J. German, C.E. Leonard, Urban air mobility: A comprehensive review and comparative analysis with autonomous and electric ground transportation for informing future research, Transportation Research Part C: Emerging Technologies, Vol. 132, 2021, 1–31, doi:10.1016/j.trc.2021.103377

[4] E.L. de Angelis, F. Giulietti, Dynamic stability and control of rotorcraft for suspended load transportation: an analytical approach, 94, 48th European Rotorcraft Forum, 6–8 Sept., 2022, pp. 1–14.

[5] D. Schneider, The delivery drones are coming, IEEE Spectrum, Vol. 57, No. 1, 2020, 28–29, doi: 10.1109/MSPEC.2020.8946304

[6] E.L. de Angelis, et al., Swing angle estimation for multicopter slung load applications, Aerosp. Sci. Technol., Vol. 89, 2019, 264–274, doi: 10.1016/j.ast.2019.04.014

[7] F. Causa, G. Fasano, Multiple UAVs trajectory generation and waypoint assignment in urban environment based on DOP maps, Aerosp. Sci. Technol., Vol. 110, 2021, 1–15, doi:10.1016/j.ast.2021.106507

[8] W. Dai, B. Pang, K.H. Low, Conflict-free four-dimensional path planning for urban air mobility considering airspace occupancy, Aerosp. Sci. Technol., Vol. 119, 2021, 1–17, doi:10.1016/j.ast.2021.107154

[9] K. Schweiger, F. Knabe, B. Korn, An exemplary definition of a vertidrome's airside concept of operations, Aerosp. Sci. Technol., in press.

[10] S.A.M. Shihab, et al., By Schedule or On Demand? - A Hybrid Operation Concept for Urban Air Mobility, AIAA Aviation 2019 Forum, AIAA 2019-3522, 2019, 1–13, doi:10.2514/6.2019-3522

[11] J.H. Boelens, The road-map to scalable urban air mobility, Volocopter white paper, 2021, 1–52, <https://www.volocopter.com/content/uploads/Volocopter-WhitePaper-2-0.pdf> (accessed 11/23/2021).

[12] E.L. de Angelis, et al., Optimal autonomous multirotor motion planning in an obstructed environment, Aerosp. Sci. Technol., Vol. 87, 2019, 379–388, doi: 10.1016/j.ast.2019.03.017

[13] E.L. de Angelis, F. Giulietti, G. Avanzini, Optimal cruise performance of a conventional helicopter, Proc. of the Institution of Mechanical Engineers, Part G: J. of Aerospace Engineering, June 2021, 1–14, doi: 10.1177/09544100211024091

[14] M. Hardesty, D. Guthrie, D. Cerchie, Unmanned Little Bird Testing Approach, 2009 American Helicopter Society International Technical Specialists Meeting on Unmanned Rotorcraft Systems, 2009, 1–12.

[15] J. Downs, et al., Control System Development and Flight Test Experience with the MQ–8B Fire Scout Vertical Take-Off Unmanned Aerial Vehicle (VTUAV), American Helicopter Society 63rd Annual Forum, 2007, 1–27.

[16] M.H. Mansur, et al., Full flight envelope inner-loop control law development for the unmanned K–MAX, American Helicopter Society 67th Annual Forum, 2011, 1–17.

[17] D. Perry, Eurocopter demonstrates unmanned EC145, Flight Global, 2013, <https://www.flightglobal.com/video-eurocopter-demonstrates-unmanned-ec145/109550.article> (accessed 11/23/2021).

[18] E. Adams, A Tap–to–Fly Helicopter Shows How Flying Cars Might Take Off, Wired, 2019, <https://www.wired.com/story/sikorsky-sara-helicopter-autonomous-flying-car-air-taxi-tech/> (accessed 11/23/2021).

[19] Curti Costruzioni Meccaniche, The new Zefhir helicopter by Curti Aerospace Division, <https://www.zefhir.eu> (accessed 11/23/2021).

[20] G. Bertolani, A.D. Ryals, L. Pollini, F. Giulietti, L1 adaptive speed control of a helicopter, 88, 48th European Rotorcraft Forum, 6–8 Sept., 2022, pp. 1–11.

[21] M.D. Pavel, G. Bertolani, F. Giulietti, Non–linear (incremental) backstepping control applied to helicopter flight, 61, 48th European Rotorcraft Forum, 6–8 Sept., 2022, pp. 1–11.

[22] M. Huber, Zefhir Successfully Tests Whole Helicopter Parachute, AINonline, 2018, <https://www.ainonline.com/aviation-news/general-aviation/2018-09-28/zefhir-successfully-tests-whole-helicopter-parachute> (accessed 11/23/2021).

[23] E. Head, How Curti put a parachute on its Zefhir helicopter, Vertical, 2019, <https://verticalmag.com/news/curti-parachute-zefhir-helicopter/> (accessed 11/23/2021).

[24] D. Talbot, et al., A Mathematical Model of a Single Main Rotor Helicopter for Piloted Simulation, NASA Technical Memorandum 84281, Sept. 1982, 1–55.

[25] Department of Defense, World Geodetic System 1984 - Its Definition and Relationship with Local Geodetic Systems, DMA Technical Report 8350.2, Sept. 1991, 1–170.

[26] U.S. Government Printing Office, U.S. Standard Atmosphere, NOAA-S/T 76-1562, Washington, D.C., 1976, 1–241.

[27] J.G. Leishman, Principles of Helicopter Aerodynamics, 2nd Edition, Cambridge University Press, New York, 2006, Chs. 2 and 5.

[28] G.D. Padfield, Helicopter Flight Dynamics, 2nd Edition, Blackwell Pub., Oxford, 2007, Ch. 3.

[29] T.R. Scavo, J.B. Thoo, On the geometry of Halley's method, The American Mathematical Monthly, Vol. 102, No. 5, 1995, 417–426, doi:10.2307/2975033

[30] J.W. Jewel, H.H. Heyson, Charts of the Induced Velocities Near a Lifting Rotor, NASA Memorandum 4-15-59L, May 1959, 1–68.

[31] J.R. Dormand, P.J. Prince, A family of embedded Runge-Kutta formulae, J. Computational and Applied Mathematics, Vol. 6, No. 1, 1980, 19–26, doi: 10.1016/0771-050X(80)90013-3

[32] W. Johnson, Helicopter Theory, Dover Publications, Inc., New York, 1994, Ch. 12.

[33] M.B. Tischler, et al., Advances in Aircraft Flight Control, 1st Edition, Taylor & Francis, London, 1996, Ch. 2, doi:10.1201/9781315136820

[34] M.B. Tischler, et al., Demonstration of Frequency Sweep Testing Technique Using a Bell 214–ST Helicopter, NASA Technical Memorandum 89422, 1987, 1–74.

[35] L. Ljung, Prediction error estimation methods, Circuits Systems and Signal Process, Vol. 21, 2002, 11–21, doi:10.1007/BF01211648

[36] G. Cai, Design and implementation of a hardware–in–the–loop simulation system for small–scale UAV helicopters, 2008 IEEE International Conference on Automation and Logistics, Vol. 21, 2008, 29–34, doi: 10.1109/ICAL.2008.4636114